Optics and Lasers in Engineering 134 (2020) 106233

Contents lists available at ScienceDirect

Optics and Lasers in Engineering

journal homepage: www.elsevier.com/locate/optlaseng

Transport of intensity equation from a single intensity image via deep learning

Kaiqiang Wang[a,1], Jianglei Di[a,1], Ying Li[a], Zhenbo Ren[a], Qian Kemao[b], Jianlin Zhao[a,*]

[a] MOE Key Laboratory of Material Physics and Chemistry under Extraordinary Conditions, Shaanxi Key Laboratory of Optical Information Technology, School of Physical Science and Technology, Northwestern Polytechnical University, Xi'an 710072, China
[b] School of Computer Science and Engineering, Nanyang Technological University, Singapore 639798, Singapore

ARTICLE INFO

Keywords:
Phase retrieval
Phase measurement
Deep learning
Neural networks

ABSTRACT

The transport of intensity equation (TIE) is an ideal candidate for phase imaging with partially coherent illuminations. TIE has the advantages of simplicity in phase calculation due to its closed-form solution and no requirement for a reference beam and phase unwrapping due to its non-interferometric nature. However, TIE requires multiple through-focus intensity images, and is very sensitive to image boundaries and noise. Thus, in this paper, we combine deep learning with TIE, abbreviated as dTIE. After being trained by TIE phase results, the dTIE retains the advantages of TIE, and overcomes the shortcomings of TIE as follows: (i) only one de-focus intensity image is required for phase imaging while the result is very close to the TIE result with SSIM index reaches 0.95, enabling more efficient phase imaging; (ii) the boundary problem automatically disappears due to the translation invariance of the convolutional networks; (iii) it is insensitive to noise even with very heavy noise. All these enhancements are verified in the application of dTIE for phase imaging of real cells.

1. Introduction

Human eyes and optical image sensors, such as charge coupled device (CCD) or complementary metal oxide semiconductor (CMOS), are sensitive to light intensity but cannot directly perceive phase information. Thus, many phase measurement techniques have been developed for both coherent and partially coherent illuminations. For example, digital holography is a typical technique for the coherent illumination, which numerically reconstructs an object wave from a hologram recorded by CCD or CMOS [1]; the transport of intensity equation (TIE) is a classic method for partially coherent illumination, which calculates the phase from multiple intensity images in a closed form [2]. TIE has been theoretically improved [3–7] and widely used in quantitative microscopic phase imaging [8–15]. In addition to the suitability for partially coherent illumination, TIE is also simple in calculation, free from reference beam and phase unwrapping, easy for the deployment to an off-the-shelf microscope [3–15]. However, TIE requires multiple intensity images for phase computation and is sensitive to noise and image boundaries [2]. Although a method has been proposed for TIE to extract phase from a single de-focused image, the assumption of 'homogeneous object' is required [16].

In recent years, deep learning has shown great potential in phase imaging [17–29], with applications in digital holography [17–26], Fourier ptychographic microscopy [27,28] and low photon count phase retrieval [29]. It is known that the undulating surface of a transparent object will change the direction of light transmission, resulting in a corresponding intensity distribution at de-focus image plane [30]. Furthermore, the complex field can be found from a set of acquired de-focus images [29]. Thus, there is a mapping relationship between the intensity and phase distributions of the object. If the intensity and phase distributions of samples can be obtained as a dataset, it will be possible for a deep learning network to learn this mapping relationship. A similar example has illustrated its feasibility, in which the phase image is reconstructed from the diffraction intensity image via a network [17]. In this paper, we propose to combine deep learning with TIE (dTIE) for phase imaging with an off-the-shelf halogen-lamp-illuminated optical microscope. First of all, a general dTIE structure (basic dTIE) is proposed where three through-focus intensity images and their TIE phase are used for network training. After training, the network is able to directly obtain phase results that are highly close to TIE with SSIM index reaches 0.96. Thus, dTIE combining with an off-the-shelf optical microscope under partially coherent illumination is achieved. Furthermore, by reducing the input images from three to only one, the basic dTIE is further developed into the enhanced dTIE. In addition, the challenging boundary and noise problems are solved and then showcase in the scenario of the enhanced dTIE.

* Corresponding author.
E-mail addresses: mkmqian@ntu.edu.sg (Q. Kemao), jlzhao@nwpu.edu.cn (J. Zhao).
[1] These authors equally contributed to this work

https://doi.org/10.1016/j.optlaseng.2020.106233
Received 13 January 2020; Received in revised form 26 March 2020; Accepted 25 May 2020

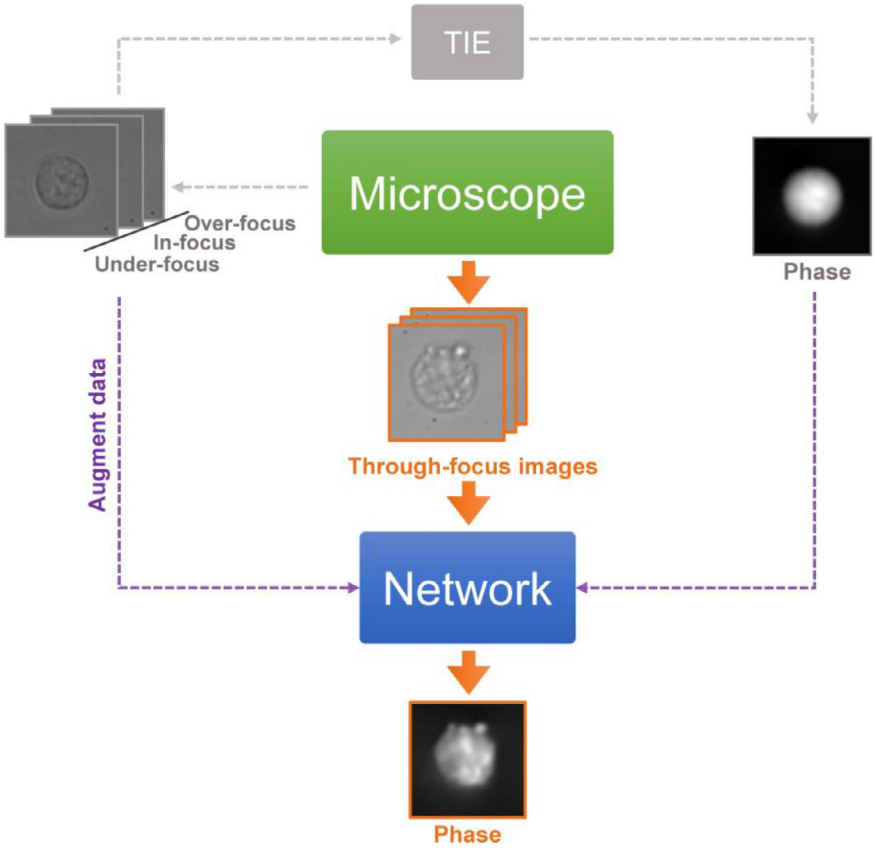

Fig. 1. Implementation diagram of dTIE.

2. Basic dTIE

Since the propose dTIE combines TIE (software) with an off-the-shelf optical microscope (hardware), and involves a training step, it is necessary to describe the overall structure of dTIE first. Also note that, although this structure is general, each component, such as the microscope and network structure, is specified to prepare for the experimental verification later on. Such a combination platform, to the best of our knowledge, has not been seen in the literature.

2.1. Overall structure

The overall structure of dTIE is shown in Fig. 1. The hardware (green block) is an off-the-shelf halogen-lamp-illuminated microscope which will be described in Section 2.2. The rest of the system is software, where the core part is neural network (blue block) for phase recovery. In order to collect data to train the network, we first capture three through-focus intensity images for each of many samples, and extract the corresponding phase images by TIE as illustrated by gray arrows, which will be detailed in Section 2.3. The network architecture (blue block) is described in detail in Section 2.4. The network is trained using the TIE phase results (purple arrows) and then used for phase recovery from all the through-focus intensity images of an unseen sample (orange arrows), whose details are given in Section 2.5. This system features the convenient adoption of an off-the-shelf optical microscope and a seamless integration of TIE and deep learning neural network for the phase imaging from a single de-focus intensity image.

2.2. Imaging hardware

An off-the-shelf inverted microscope (XDS-3) is used for our hardware setup, as shown in Fig. 2. The illumination light source is a halogen lamp, whose spatial coherence is determined by the size of the condenser aperture, which can be represented by coherent parameter S (i.e., the ratio of the condenser aperture to the objective numerical aperture). In our experiment, the condenser aperture is adjusted to $S \approx 0.3$ to ensure sufficient coherence while reducing the coherent noise [12]. The central wavelength of the filtered illumination source is 550 nm. The sample is placed on a motorized translation platform with an axial minimum step size of 50 nm. The beam passes through the sample and carries the sample's phase information. Then the beam is focused by $a \times 40/0.65$ NA objective, and captured by a CCD camera through a tube lens. The depth of field of the microscope is 0.99 μm. Note that such a hardware setup is general and easily implementable for phase imaging.

2.3. Data capturing and tie phase extraction

The live mouse phagocytes are used as samples in the above setup. These samples are maintained in a humidified incubator at 37 °C and 5% CO_2 in Dulbecco's modified eagle medium (DMEM) supplemented with 10% heat-inactivated fetal bovine serum and 1% penicillin-streptomycin mixture. After attaching to the bottom of a culture dish, 1643 cells are imaged one by one. During imaging, each cell is ensured to be in the center of the field of view to meet the homogeneous Neumann boundary condition for TIE, and the through-focus intensity images are captured as $I(x, y, \Delta z)$, $I(x, y, 0)$ and $I(x, y, -\Delta z)$, respectively. Then all these through-focus intensity images are normalized to remove the influence of different light intensities [31]. The in-focus intensity image plane is found by the autofocus function [32]. The corresponding phase images can now be recovered by TIE.

The phase recovery by TIE is standard and is briefly explained for the completeness of this paper. TIE provides the following relationship,

$$-k\frac{\partial I(x,y,z)}{\partial z} = \nabla \cdot [I(x,y,z)\nabla\varphi(x,y,z)], \tag{1}$$

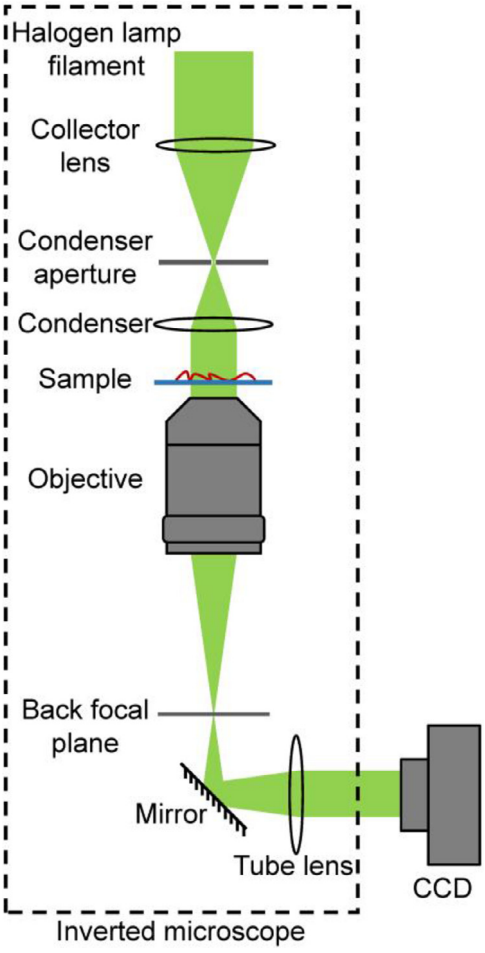

Fig. 2. Experimental setup.

where (x, y) represents transverse spatial coordinates perpendicular to the optical axis, while z is along the optical axis, $\varphi(x, y, z)$ is the phase distribution of the sample, ∇ is the two-dimensional gradient with respect to x and y, and $k = 2\pi/\lambda$ is the wave number. The phase is extracted as

$$\varphi(x, y, z) = -k\nabla^{-2}\nabla \cdot \left[\frac{1}{I(x, y, z)}\nabla\nabla^{-2}\frac{\partial(x, y, z)}{\partial z}\right], \tag{2}$$

where ∇^{-2} is inverse Laplacian operator, which can be implemented with the use of fast Fourier transform (FFT) algorithm under the homogeneous Neumann boundary condition [33]. The derivative of the image intensity is approximated by finite difference as

$$\frac{\partial(x, y, z)}{\partial z} \approx \frac{I(x, y, \Delta z) - I(x, y, -\Delta z)}{2\Delta z}, \tag{3}$$

which is simple but introduces a nonlinear error [34]. In order to reduce noise as much as possible, the experimental environment is carefully controlled to be dust- and vibration- free. In view of the influence of noise on TIE, we choose the minimum de-focus distance (Δz = 2 μm) while ensuring that the intensity difference is not affected by noise [34]. For complex samples, involving more de-focus intensity images is more suitable [35] and will be tested in our future study.

The through-focus intensity images and the TIE phase results of each cell are used as dataset. To strengthen the generalization ability of dTIE (such as translation and rotation invariance) and extend the mapping relationship to the entire field of view, the dataset is augmented to 25,047 pairs by random translation and rotation. After that, Gaussian noise with random standard deviations from 0 to 25 is added into the through-focus intensity images of the training dataset for better robustness. Among all the dataset, 80% are used for training dataset, and 10% for validation dataset and 10% for testing dataset.

2.4. Network architecture

The architecture of neural network is inspired by U-Net [36] and residual network [37], as shown in Fig. 3. It consists of a down-sampling path in the left side, an up-sampling path in the right side, and a bridge path in the middle to connect the down- and up-sampling paths. The down-sampling path consists of four repeated stages of two 3 × 3 convolutions, a residual block [37] between the two convolutions, and a 2 × 2 max pooling operation with stride 2 following the two convolutions. The number of feature channels is increased by the first convolution in each stage of down-sampling path (the first stage is from 1 channel to 64 channels and the rest stages double the channels). The bridge path is gained by removing the max pooling operation from the down-sampling path. The up-sampling path consists of four repeated stages of an up-convolution (transposed convolution) concatenating with corresponding feature map at the down-sampling path by skip connection, two 3 × 3 convolutions and a residual block between the two convolutions. The last convolutions in each stage of up-sampling path decrease the number of the feature channels (the last stage is from 32 channels to 1 channel and the rest stages halve the channels). All the convolutions in this neural network are followed by a BN and a ReLU for faster training speed and non-linear ability [38,39].

2.5. Network training and phase recovery

The network training is shown in Fig. 4(a). All the through-focus intensity images and the TIE phase results are used as input and ground truth, respectively. The mean squared error (MSE) of the network output with ground truth is calculated and used as the loss function. Next, the loss function is back-propagated through the network and the ADAM-based optimization [40] with a learning rate of 0.001 is adopted to update the network's parameters. To avoid over-fitting of the neural network, the training stops when the network performance on the validation dataset begins to decline. This trained network is denoted as Network1 for convenience.

As shown in Fig. 4(b), after training, Network1 is randomly given a set of through-focus intensity images of the testing dataset and rapidly outputs the corresponding phase image. As a result, our proposed dTIE works successfully. We will show the results later against various improved results in the next section.

For implementing the network, TensorFlow framework version 1.1.0 based on Python 3.6.1 is used. The network training and testing are performed on a PC with Core i7–8700 K CPU (3.8 GHz) and 16 GB of RAM, using NVIDIA GeForce GTX 1080Ti GPU. The training process takes ~3 h for 100 epochs (~20,000 pairs of images size of 128 × 128 pixels in a batch size of 64). The network reconstruction time for a phase image is ~0.014 s.

2.6. Initial test of the dTIE

To observe how the neural network output changes with training epoch, in Fig. 5, we show how MSE between output and ground truth declines, and how the corresponding structural similarity (SSIM) index increases [41]. The oscillation of the curves is caused by the use of mini-batches learning at size of 64, which does not have a negative impact on the training results. More intuitively, the network outputs of an example cell in training image set are shown below the corresponding position of the x axis every four epochs (specifically, every epoch from 9th to 15th epoch) (see Visualization 1 for details). With the updating of network parameters, the output is getting closer to the ground truth with SSIM index reaches 0.95, which confirms the feasibility and initial success of the proposed dTIE.

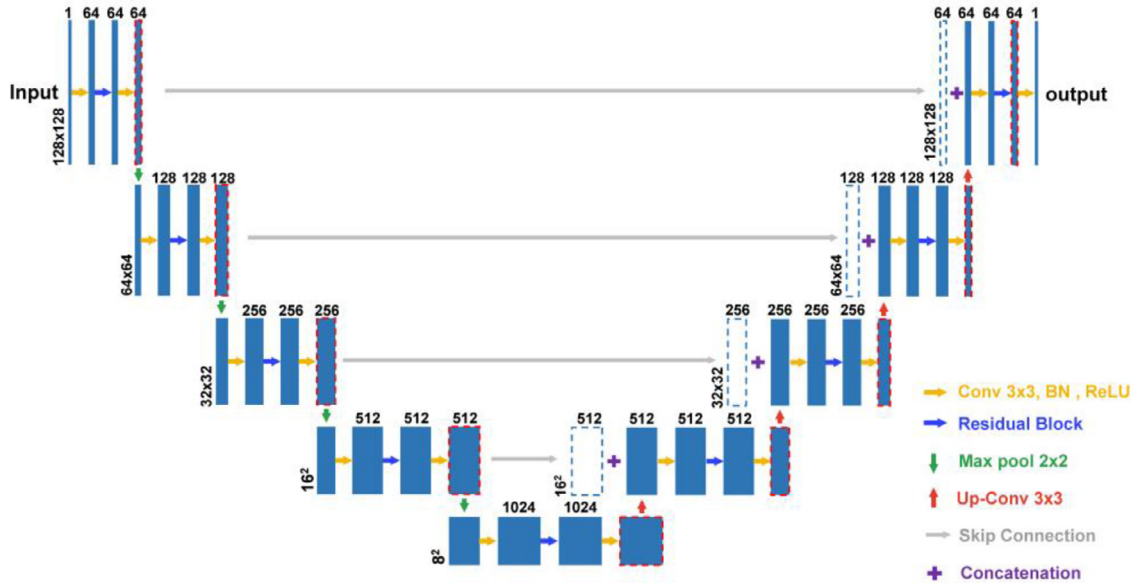

Fig. 3. Network architecture. Each blue box corresponds to a multi-channel feature map. The number of channels is provided on top of the box. The x-y-size is denoted at the lower left edge of the box. White-dotted boxes represent copied feature maps. The arrows and symbol denote different operations. Red-dotted boxes will be visualized in Fig. 7 later. (For interpretation of the references to colour in this figure legend, the reader is referred to the web version of this article.)

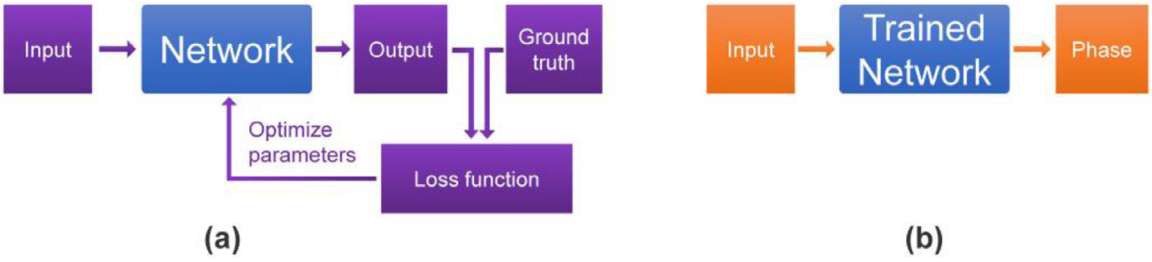

Fig. 4. Training and testing of the network1. **(a)** Network-training flow diagram, **(b)** network-testing flow diagram.

3. Enhanced dTIE

Utilizing the power of deep neural network for nonlinear mapping between de-focus image and phase, the basic dTIE is further developed into the enhanced dTIE by reducing the input images from three to only one, which is more convenient. In this section, we also highlight and showcase the power of networks in solving the challenging boundary and noise problems in the scenario of the enhanced dTIE which we promote in this paper.

3.1. Reducing the input images to only one

The TIE retrieves the phase information from intensity images in different de-focus distances. That is, the TIE method requires at least two intensity maps [13]. In fact, a single intensity image also contains the phase information of the object [17,30]. However, it is unknown and interesting to find out whether one intensity image is sufficient for successful phase recovery in the dTIE. We thus propose to train two new networks: Network+ with a single over-focus intensity image as input, and Network− with a single under-focus intensity image as input. The training processes of Network+ and Network- are the same as that of Network1.

To compare the performances of Network1, Network+ and Network−, these networks are used to reconstruct the phase images of three example cells using corresponding through-focus intensity images. As shown in Fig. 6, the phase results and their error maps compared with the ground truth demonstrate a good matching performance of these three networks with TIE, where the maximum difference is less than 0.06π. Since the three networks have the same error level and properties, we use the Network+ for following discussion. Also, the average of the results from Network+ and Network− does not improve the accuracy. More in-depth research will be carried out in the follow-up work.

In order to explore the internal mechanism of the neural network in the phase recovery process, we visualize the intermediate activation maps [42] of Network+ by inputting the over-focus intensity image of a cell in Fig. 7. The channels are partly selected from the layers marked by the red-dotted boxes in Fig. 3. The intermediate activation maps 4–16, 20 and 24–39 belong to down-sampling, bridge and up-sampling paths, respectively. The down-sampling paths contain the strong features of the intensity image such as the outline and internal details of the over-focus intensity image, etc. Meanwhile, the up-sampling paths contain the features of the phase images. Interestingly, the first to third rows seem to be learning the internal details, contour and overall distribution, respectively, in which down-sampling paths are for over-focus intensity information, bridge path is for the transition from intensity to phase, and up-sampling paths are for the phase information. Of course, in addition to the three selected channels, there are many other channels that do not have a clear and interpretable function. A similar phenomenon is also seen in Network−.

3.2. Improving the performance at image boundaries

Before solving TIE, physical or mathematical preprocess are required to satisfy the specific boundary conditions [43–46], which affects the

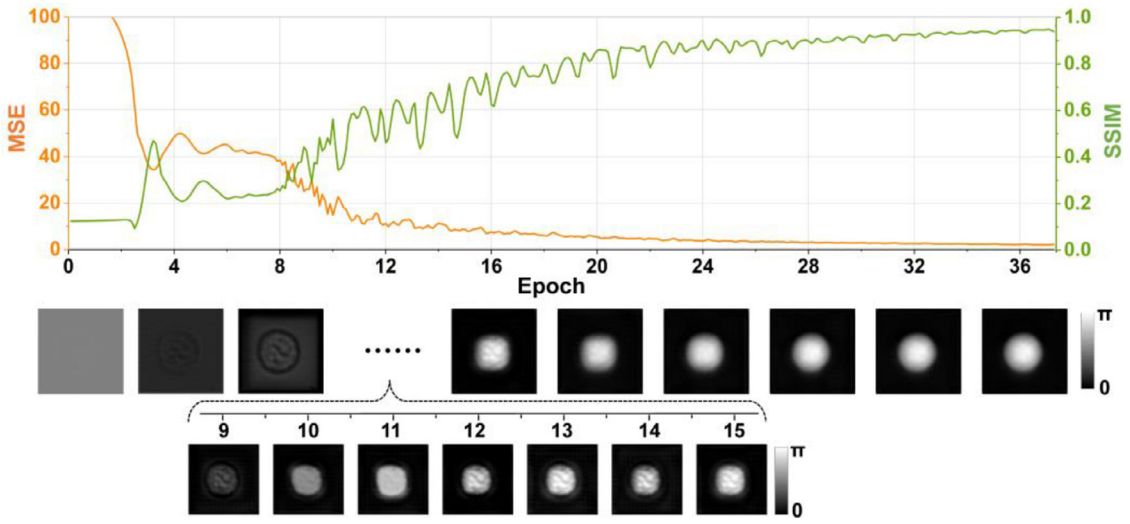

Fig. 5. MSE and SSIM index of the training imaging set as a function of the number of epochs. The network outputs of an example cell in training image set are below (see Visualization 1 for a detailed comparison).

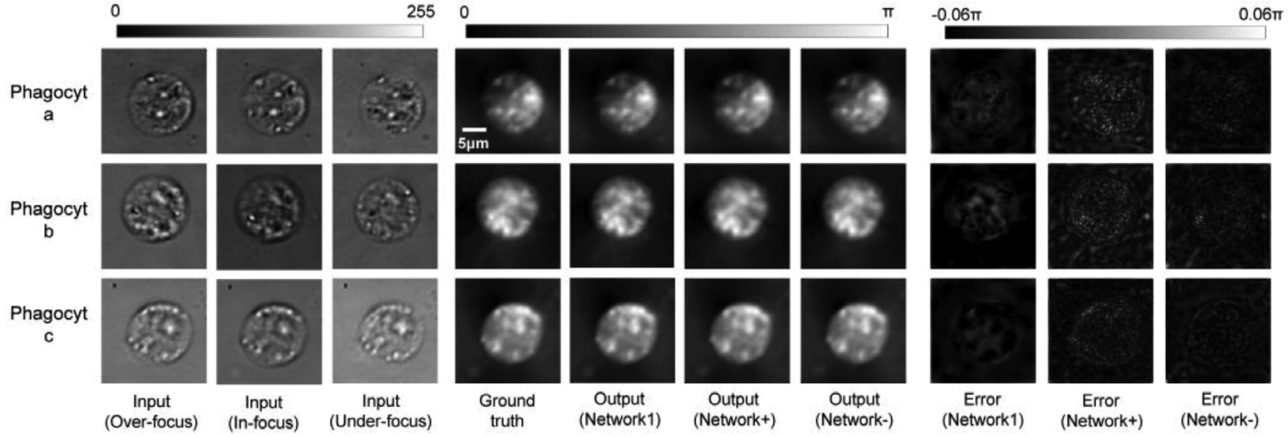

Fig. 6. Inputs, outputs, and TIE phase results (ground truth) of three test examples for Network1, Network+ and Network-.

versatility and convenience of traditional TIE methods. As for the dTIE, the convolutional network itself has certain translation invariance [47]. The data augmentation mentioned in Section 2.3 will further enhance the translation invariance of the networks.

To compare the results of enhanced dTIE and FFT-solved TIE [33] under different boundaries conditions, many through-focus intensity image sets of a cell are captured while translating the field of view from right to left. The phase images are then recovered by both network+ and TIE. The TIE result obtained when the cell is in the center of the field of view and its translation versions are used as the ground truth, because these results are not affected by the image boundaries. The phase results from network+ and TIE are compared with the ground truth by computing the SSIM indices for different cell locations, for every 5-pixel translation distance from −100th to 100th pixel, as shown in Fig. 8. The network+ produces obviously better results when the cell is slightly away from the image center. It is interesting to see that good phase recovery is achieved even when only a small portion of the cell is captured near the boundary (see Visualization 2 for details).

3.3. Anti-noise performance

We know that TIE is sensitive to noise [34]. The unique advantage of deep learning is that it is possible to learn and establish the expected mapping even from noisy inputs. The method of adding Gaussian noise to the input of the dataset mentioned in Section 2.3 further enhances the anti-noise ability of the networks.

To compare the anti-noise ability of enhanced dTIE and TIE, Gaussian noise with standard deviation from 0 to 29 is added to the over-focus intensity image of a tested cell. Then, the network+ and TIE are used to recover the phase, and we subsequently calculate their SSIM indices with the phase recovered by TIE without adding noise as the ground truth. The results are shown in Fig. 9 (see Visualization 3 for details). The network+ outperforms TIE when the noise standard deviation reaches 2.

4. Discussions

4.1. Generalization capability and accuracy analysis

To analyze the generalization capability of enhanced dTIE, the living mouse osteoblasts are used as another set of samples. Using the same network architecture depicted in Fig. 3, we trained three network+ versions with different cell types, i.e., phagocytes only, osteoblasts only, and both of them. The testing results of these networks are exemplified in Fig. 10(a), with the quantitative SSIM indices shown in Table 1. We can see that using the network trained by phagocytes to recover the phase of osteoblasts, or vice versa, produces encouraging results but is obviously inferior to that of the network trained by the same type of

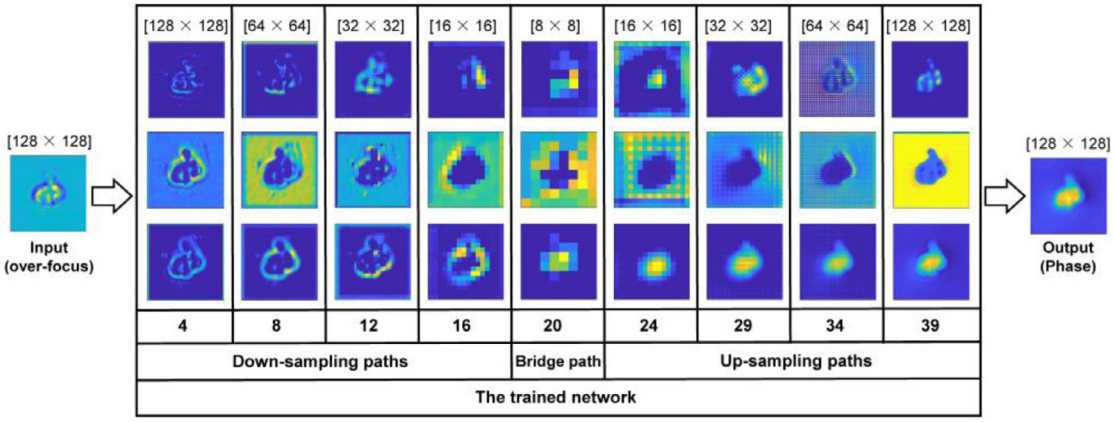

Fig. 7. Visualization of the intermediate activation maps of Network+ by inputting an over-focus intensity image of a cell. The channels are partly selected from the layers marked by the red-dotted boxes of Fig. 3. The convolution orders of the channel are as followings: 4, 8, 12, 16, 20, 24, 29, 34 and 39. (For interpretation of the references to colour in this figure legend, the reader is referred to the web version of this article.)

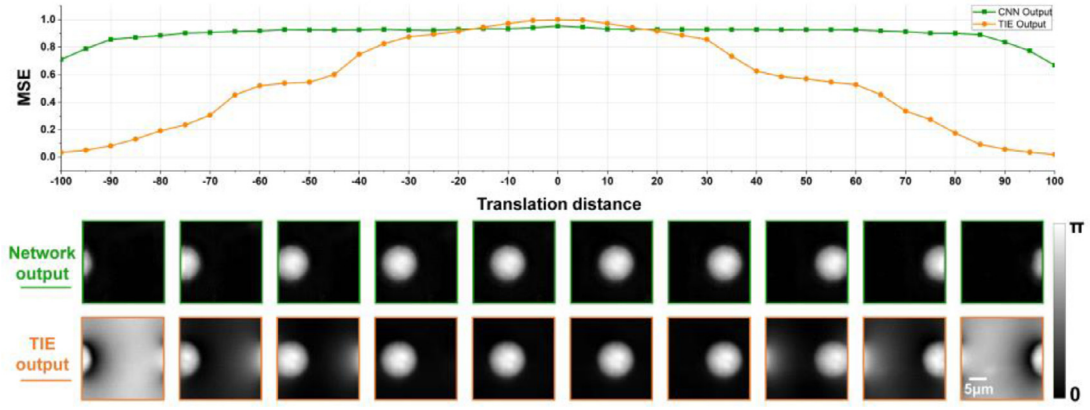

Fig. 8. SSIM index of the standard with the network and TIE outputs while translating the field of view from right to left. The network output (in the green box) and the TIE output (in the orange box) of a cell in the testing image set are below the corresponding position of the *x* axis every 20 pixels (see Visualization 2 for a detailed comparison). (For interpretation of the references to colour in this figure legend, the reader is referred to the web version of this article.)

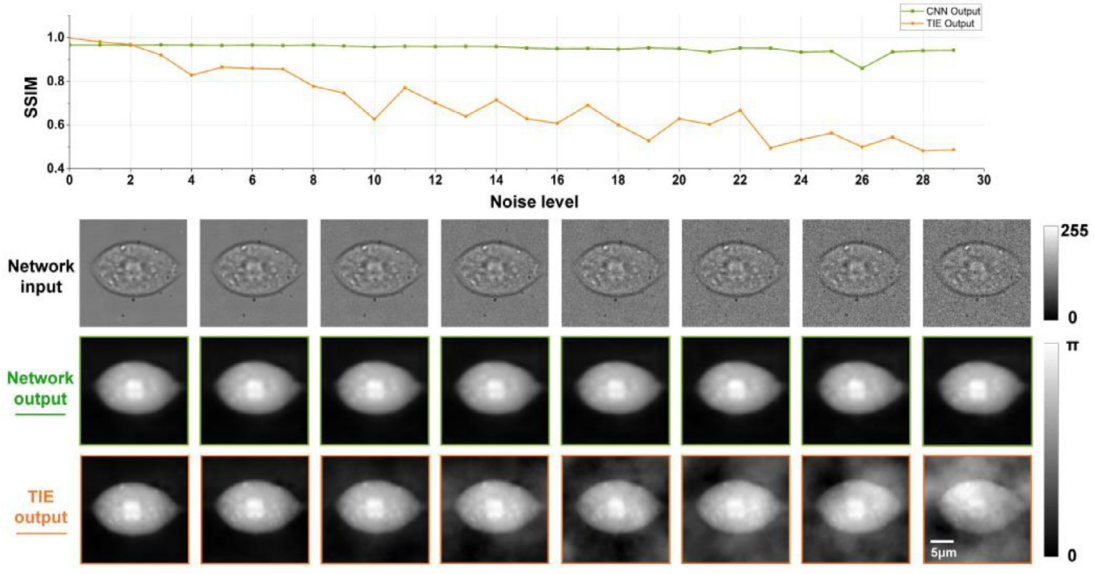

Fig. 9. SSIM index of the standard with network and TIE phase results while the standard deviations of Gaussian noise increasing from 0 to 29. The network input, the network output (in the green box) and the TIE output (in the orange box) of an example cell in the testing image set below the corresponding position of the *x* axis every 4 pixels (see Visualization 3 for a detailed comparison). (For interpretation of the references to colour in this figure legend, the reader is referred to the web version of this article.)

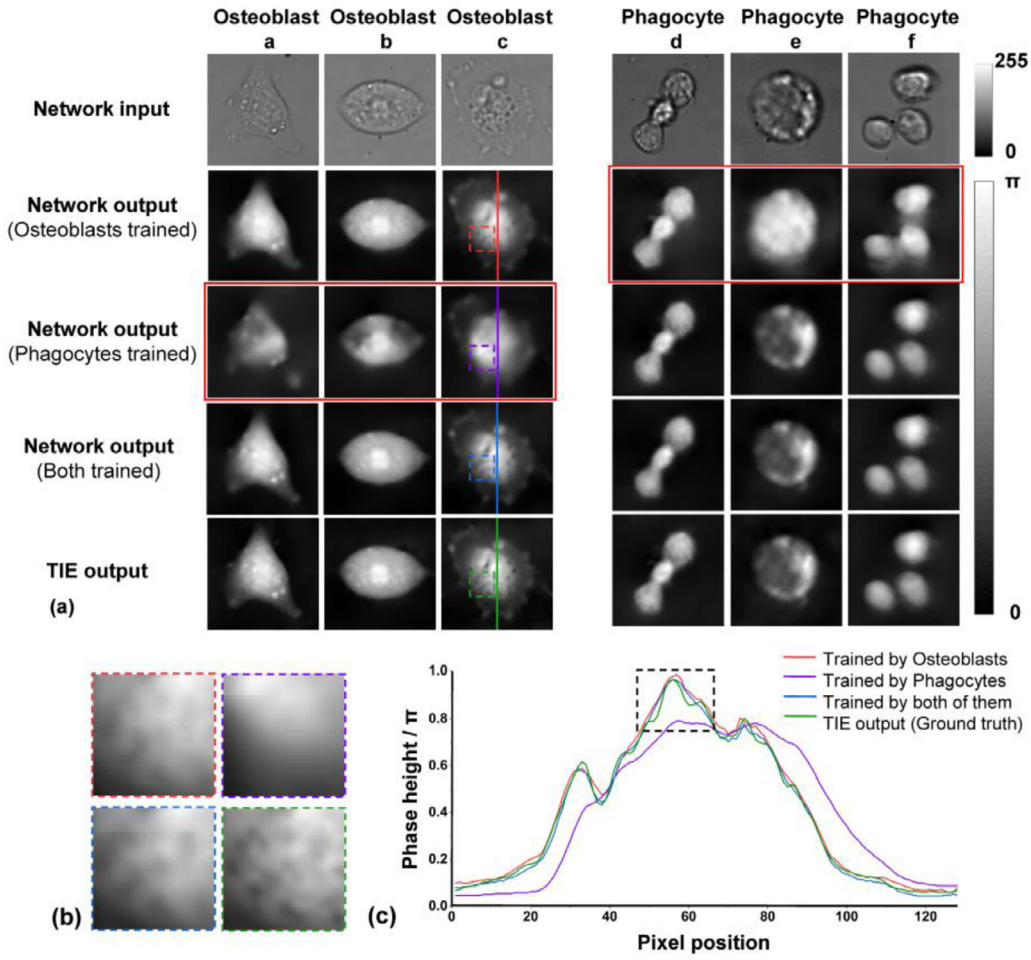

Fig. 10. Comparison of the recovered results for the specific networks trained by different types of cells and universal network trained by both types of cells. **(a)** Results comparison; **(b)** enlarged area with high-frequency information of Osteoblast c; **(c)** phase profile along lines of Osteoblast c. (For interpretation of the references to colour in this figure legend, the reader is referred to the web version of this article.)

Table 1
Comparison of the recovered results' SSIM indices for the TIE output with the specific networks trained by different types of samples and the universal networks trained by both types of samples.

Sample types / Output	Osteoblast a	Osteoblast b	Osteoblast c	Phagocyte d	Phagocyte e	Phagocyte f
Network output (Osteoblasts trained)	0.942	0.945	0.951	0.851	0.749	0.878
Network output (Phagocytes trained)	0.693	0.749	0.734	0.950	0.945	0.953
Network output (Both trained)	0.945	0.942	0.949	0.953	0.953	0.959
TIE output	1.000	1.000	1.000	1.000	1.000	1.000

tested cell. It means that, before a cell is imaged, the type of cells should have already been used to train the network. It is also observed that the universal network using both types of cells achieved the best cell-type generalization capability and is thus recommended for practical use.

In addition to cell types, the difference of de-focus amount, microscopes and illumination conditions is also the generalization factors for the network. For different de-focus amounts, the intensity distributions of the same sample are different. For different microscope systems, the optical transfer functions are different. The mapping relationship from intensity to phase learned by the network is only for a given de-focus amount and a given microscope, so in principle, specific networks or transfer learning are needed [48]. For different illumination conditions, the normalization method in [31] for the through-focus intensity images can be used to remove the influence of different light intensity.

To analyze the accuracy of enhanced dTIE, the area with high-frequency information of Osteoblast c is enlarged in Fig. 10(b) and the phase profile along lines of Osteoblast c is plotted in Fig. 10(c). As shown in Fig. 10(b), the granular structures are relatively blurry in the network outputs. Quantitatively, in Fig. 10(c), the overall distribution of network results is greatly consistent with the ground truth (TIE output) except for the network trained by phagocytes. From the black dotted box, we can see that the ground truth has three bumps; however, the neural network reconstructs the largest one. The above phenomenon shows that the reconstruction result of the neural network cannot be exactly equal

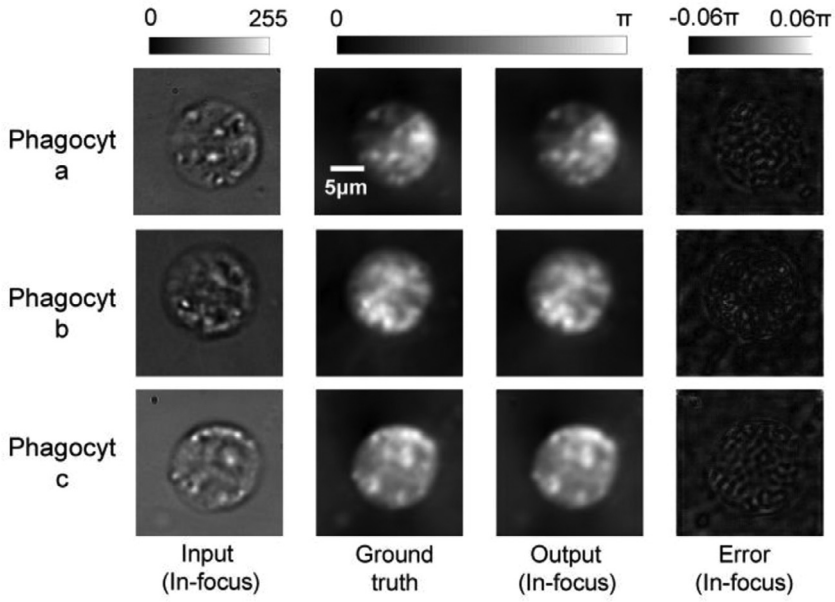

Fig. 11. Network inputs (in-focus), outputs and TIE outputs of these three test examples shown in Fig. 6.

Table 2
Comparison of the recovered results' SSIM indices for the TIE output with Network1, Network+, Network0 and Network- of three samples shown in Fig. 6 and Fig. 11.

SSIM \ Types	Phagocytes a	Phagocytes b	Phagocytes c	Mean
Network1	0.961	0.955	0.963	0.960
Network+	0.959	0.954	0.956	0.956
Network0	0.958	0.959	0.955	0.957
Network-	0.959	0.959	0.957	0.958
TIE	1.000	1.000	1.000	1.000

to the ground truth, but has some loss of detail information, resulting from a common phenomenon in deep learning that the loss function of the neural network cannot converge to zero but can only be close to a number greater than zero.

4.2. In-focus intensity images for phase recovery

We also attempted to train a network by the in-focus intensity images and TIE phase results as input and ground truth, and call it Network0. As shown in Fig. 11, the range of its error maps is from -0.06π to 0.06π which is the same with that of the Network1, Network+ and Network− shown in Fig. 6. Interestingly, as seen in Table 2, the mean SSIM indices of these four networks are almost exactly the same (0.960 for Network1, 0.956 for Network+, 0.958 for Network−, 0.957 for Network0). We attribute this phenomenon to a much higher cell height (~5 μm) than the depth of field (0.98 μm) of the microscope, which is called a thick cell situation. We mention this interesting phenomenon for further investigation.

Conclusion

Phase imaging from the intensity image with off-the-shelf halogen-lamp-illuminated has been demonstrated by the proposed dTIE. While retaining all the advantages of TIE such as adaptability for partially coherent illumination, simplicity for phase calculation and no requirement for a reference beam and phase unwrapping, the dTIE improves the weaknesses of TIE which are highlighted as follows: reducing the required intensity images from multiple to one, being free from the image boundary problem and being more insensitive to noise. An off-the-shelf microscope which can only be used for intensity microscopy, once directly combined with the dTIE, can provide another function of phase imaging. We believe that the dTIE has great application prospects.

Funding

National Natural Science Foundation of China (NSFC) (61927810); The Joint Fund of the National Natural Science Foundation of China and the China Academy of Engineering Physics NSAF (U1730137); The Fundamental Research Funds for the Central Universities (3102019ghxm018).

Declaration of Competing Interest

This manuscript is approved by all authors for publication. I would like to declare on behalf of my co-authors that the work described was original research that has not been published previously, and not under consideration for publication elsewhere, in whole or in part.

Supplementary materials

Supplementary material associated with this article can be found, in the online version, at doi:10.1016/j.optlaseng.2020.106233.

CRediT authorship contribution statement

Kaiqiang Wang: Conceptualization, Methodology, Software, Visualization, Writing - original draft. **Jianglei Di:** Conceptualization, Project administration, Funding acquisition, Writing - review & editing. **Ying Li:** Investigation, Resources. **Zhenbo Ren:** Writing - review & editing. **Qian Kemao:** Writing - review & editing, Supervision. **Jianlin Zhao:** Writing - review & editing, Supervision, Funding acquisition.

References

[1] Cuche E, Bevilacqua F, Depeursinge C. Digital holography for quantitative phase–contrast imaging. Opt. Lett. 1999;24:291–3.
[2] Reed TM. Deterministic phase retrieval: a Green's function solution. JOSA 1983;73:1434–41.
[3] Gureyev TE, Roberts A, Nugent KA. Partially coherent fields, the transport-of-intensity equation, and phase uniqueness. J. Opt. Soc. Am. A 1995;12:1942–6.
[4] Paganin D, Nugent KA. Noninterferometric phase imaging with partially coherent light. Phys. Rev. Lett. 1998;80:2586–9.
[5] Gureyev TE, Nugent KA. Rapid quantitative phase imaging using the transport of intensity equation. Opt. Commun. 1997;133:339–46.
[6] Zysk AM, Schoonover RW, Carney PS, Anastasio MA. Transport of intensity and spectrum for partially coherent fields. Opt. Lett. 2010;35:2239–41.
[7] Petruccelli JC, Tian L, Barbastathis G. The transport of intensity equation for optical path length recovery using partially coherent illumination. Opt. Express 2013;21:14430–41.
[8] Barty A, Nugent KA, Paganin D, Roberts A. Quantitative optical phase microscopy.. Opt. Lett. 1998;23:817–19.
[9] Kou SS, Waller L, Barbastathis G, Sheppard CJR. Transport-of-intensity approach to differential interference contrast (TI-DIC) microscopy for quantitative phase imaging. Opt. Lett. 2010;35:447–9.
[10] Yang F, Wang Z, Wen Y, Qu W. A quantitative phase imaging system based on transport-of-intensity equation. In: Proc. SPIE 9524, International Conference on Optical and Photonic Engineering (icOPEN 2015); 17 July 2015. 952424.
[11] Li J, Xu J, Zhong L, Zhang Q, Wang H, Tian J, et al. An orthogonal direction iterative algorithm of the transport-of-intensity equation. Opt Lasers Eng 2019;120:6–12.
[12] Zuo C, Chen Q, Qu W, Asundi A. Noninterferometric single-shot quantitative phase microscopy. Opt. Lett 2013;38:3538–41.
[13] Li Y, Di J, Ma C, Zhang J, Zhong J, Wang K, Xi T, Zhao J. Quantitative phase microscopy for cellular dynamics based on transport of intensity equation. Opt. Express 2018;26:586–93.
[14] Zhang H, Zhou W, Liu Y, Tian T, Banerjee P, Poon T. Finite Difference Approach to Transport of Intensity. Digital Holography and Three-Dimensional Imaging. OSA Technical Digest (online) (Optical Society of America; 2017. paper W1A.5.
[15] Zhou W, Guan X, Liu F, Yu Y, Zhang H, Poon T, Banerjee P. Phase retrieval based on transport of intensity and digital holography. Appl. Opt. 2018;57:A229–34.
[16] Paganin D, Mayo SC, Gureyev TE, Miller PR, Wilkins SW. Simultaneous phase and amplitude extraction from a single defocused image of a homogeneous object. J. Microsc. 2002;206:33–40.
[17] Sinha A, Lee J, Li S, Barbastathis G. Lensless computational imaging through deep learning. Optica 2017;4:1117–25.
[18] Horisaki R, Takagi R, Tanida J. Deep-learning-generated holography. Appl. Opt 2018;57:3859–63.
[19] Rivenson Y, Zhang Y, Günaydın H, Teng D, Ozcan A. Phase recovery and holographic image reconstruction using deep learning in neural networks. Light Sci. Appl. 2018;7:17141.
[20] Wu Y, Rivenson Y, Zhang Y, Wei Z, Günaydin H, Lin X, et al. Extended depth-of-field in holographic imaging using deep-learning-based autofocusing and phase recovery. Optica 2018;5:704–10.
[21] Ren Z, Xu Z, Lam EY. Learning-based nonparametric autofocusing for digital holography. Optica 2018;5:337–44.
[22] Pitkäaho T, Manninen A, Naughton TJ. Focus prediction in digital holographic microscopy using deep convolutional neural networks. Appl. Opt. 2019;58:A202–8.
[23] Wang K, Li Y, Kemao Q, Di J, Zhao J. One-step robust deep learning phase unwrapping. Opt. Express 2019;27:15100–15.
[24] Wang H, Lyu M, Situ G. eHoloNet: a learning-based end-to-end approach for in-line digital holographic reconstruction. Opt. Express 2018;26:22603–14.
[25] Ren Z, Xu Z, Lam EY. End-to-end deep learning framework for digital holographic reconstruction. Adv. Photon. 2019;1:016004.
[26] Wang K, Dou J, Kemao Q, Di J, Zhao J. Y-Net: a one-to-two deep learning framework for digital holographic reconstruction. Opt. Lett. 2019;44:4765–8.
[27] Xue Y, Cheng S, Li Y, Tian L. Reliable deep-learning-based phase imaging with uncertainty quantification. Optica 2019;6:618–29.
[28] Nguyen T, Xue Y, Li Y, Tian L, Nehmetallah G. Deep learning approach for Fourier ptychography microscopy. Opt. Express 2018;26:26470–84.
[29] Goy A, Arthur K, Li S, Barbastathis G. Low photon count phase retrieval using deep learning. Phys. Rev. Lett. 2018;121:243902.
[30] Nugent KA. The measurement of phase through the propagation of intensity: an introduction. Contemp Phys 2011;52:55–69.
[31] Mudrak NJ, Rana PS, Model MA. Calibrated brightfield-based imaging for measuring intracellular protein concentration. Cytom. Part A 2017;93:297–304.
[32] Santos A, Ortiz de Solórzano C, Vaquero JJ, Pena JM, Malpica N, Del Pozo F. Evaluation of autofocus functions in molecular cytogenetic analysis. J. Microsc. 1997;188:264–72.
[33] Allen LJ, Oxley MP. Phase retrieval from series of images obtained by defocus variation. Opt. Commun. 2001;199:65–75.
[34] Paganin D, Barty A, McMahon PJ, Nugent KA. Quantitative phase-amplitude microscopy. III. The effects of noise.. J. Microsc. 2004;214:51–61.
[35] Waller L, Tian L, Barbastathis G. Transport of intensity phase-amplitude imaging with higher order intensity derivatives. Opt. Express 2010;18:12552–61.
[36] Ronneberger O, Fischer P, Brox T. U-net: convolutional networks for biomedical image segmentation. In: International Conference on Medical Image Computing and Computer-assisted Intervention. Springer; 2015. p. 234–41.
[37] He K, Zhang X, Ren S, Sun J. Deep residual learning for image recognition. In: Proceedings of IEEE Conference on Computer Vision and Pattern Recognition. IEEE; 2016. p. 770–8.
[38] S. Ioffe and C. Szegedy. Batch normalization: accelerating deep network training by reducing internal covariate shift. arXiv preprint arXiv:1502.03167 (2015).
[39] Glorot X, Bordes A, Bengio Y. Deep sparse rectifier neural networks. In: Proceedings of the Fourteenth International Conference on Artificial Intelligence and Statistics; 2011. p. 315–23. Academic.
[40] D.P. Kingma and J. Ba. Adam: A method for stochastic optimization. arXiv preprint arXiv: 1412.6980 (2014).
[41] Wang Z, Bovik AC, Sheikh HR, Simoncelli EP. Image quality assessment: from error visibility to structural similarity. IEEE Trans. Image Process 2004;13:600–12.
[42] Zeiler MD, Fergus R. Visualizing and understanding convolutional networks. In: European Conference on Computer Vision. Springer; 2014. p. 818–33.
[43] Gilbarg D, Trudinger NS. Elliptic partial differential equations of second order. springer; 2015.
[44] Volkov VV, Zhu Y, De Graef M. A new symmetrized solution for phase retrieval using the transport of intensity equation. Micron 2002;33:411–16.
[45] Martinez-Carranza J, Falaggis K, Kozacki T, Kujawinska M. Effect of imposed boundary conditions on the accuracy of transport of intensity equation based solvers. Proc. SPIE 2013;8789:87890N.
[46] Zuo C, Chen Q, Asundi A. Boundary-artifact-free phase retrieval with the transport of intensity equation: fast solution with use of discrete cosine transform. Opt. Express 2014;22:9220–44.
[47] Goodfellow I, Bengio Y, Courville A. Deep learning. Massachusetts: Institute of Technology; 2016.
[48] Pan SJ, Yang Q. A survey on transfer learning. IEEE Trans Knowl Data Eng 2009;22:1345–59.